Structural studies of mesoporous ZrO$_2$-CeO$_2$ and ZrO$_2$-CeO$_2$/SiO$_2$ mixed oxides for catalytical applications

R. Bacani [a, *], T.S. Martins [b], M.C.A. Fantini [a], D.G. Lamas [c]

[a] Departamento de Física Aplicada, Instituto de Física, Universidade de São Paulo, Travessa R da Rua do Matão, No. 187, Cidade Universitária, 05508-090, São Paulo, Brazil
[b] Departamento de Ciências Exatas e da Terra, Instituto de Ciências Ambientais, Químicas e Farmacêuticas, Universidade Federal de São Paulo - UNIFESP, Rua São Nicolau, 210, 2o Andar, Diadema, 09913-030, São Paulo, Brazil
[c] CONICET / Escuela de Ciencia y Tecnología, Universidad Nacional de General San Martín, Martín de Irigoyen 3100, Edificio Tornavía, Campus Miguelete, (1650) San Martín Pcia, de Buenos Aires, Argentina

ARTICLE INFO

ABSTRACT

In this work the synthesis of ZrO$_2$-CeO$_2$ and ZrO$_2$-CeO$_2$/SiO$_2$ were developed, based on the process to form ordered mesoporous materials such as SBA-15 silica. The triblock copolymer Pluronic P-123 was used as template, aiming to obtain crystalline single phase walls and larger specific surface area, for future applications in catalysis. SAXS and XRD results showed a relationship between ordered pores and the material crystallization. 90% of CeO$_2$ leaded to single phase homogeneous ceria-zirconia solid solution of cubic fluorite structure (Fm$\overline{3}$ m). The SiO$_2$ addition improved structural and textural properties as well as the reduction behavior at lower temperatures, investigated by XANES measurements under H$_2$ atmosphere.

© 2016 Elsevier B.V. All rights reserved.

1. Introduction

Mesoporous materials have interesting properties, such as high surface area, adjustable size and shape of pores, several different structures and compositions which provide potential applications in catalysis, adsorption, sensors, drug delivery and nanodevices [1]. The extension of silicon-based materials synthesis to other metal oxides is extensively pursued, since ordered mesoporous materials such as MCM-41 and SBA-15 present excellent textural/structural properties [1–6].

Zirconia-Doped Ceria (ZrO$_2$-x%CeO$_2$, ZDC) is a largely studied solid solution due to its physical-chemical properties that are useful for applications in three-way catalysts and as anodes in Solid Oxide Fuel Cells (SOFC). Among these properties, a high surface area is pursued since the gas permeation in the material allows a high gas reaction rate. Also, ceria-based materials present the ability to store/release oxygen during rich/poor fuel conditions, which is correlated to the Ce^{4+} ↔ Ce^{3+} redox reaction [7–12].

Several authors reported the synthesis of mesoporous ceria-zirconia materials [13–18] but few presented a detailed study of the porous network via SAXS and the evolution of the pore ordering, regarding the materials crystallization. Therefore, the aim of this work was to explore different synthesis methods to produce ZDC samples and fully characterize their physical chemical properties for future applications. In particular, the strategy to build a SiO$_2$ palisade was analyzed as an attempt to avoid shrinkage during calcination.

2. Experimental

2.1. ZrO$_2$-CeO$_2$ and ZrO$_2$-CeO$_2$/SiO$_2$ preparation

Anhydrous chloride method: 2 g of Pluronic P-123 (BASF) was previously stirred in 10 mL of ethanol, a total of 13.8 mmol of anhydrous ZrCl$_4$ and CeCl$_3$ (Aldrich) were solubilized in another 10 mL of ethanol and added to the polymer mixture (Ce/Zr molar ratios of 0.5 and 0.9). Approximately 2 mL of water were added to the solution, and the Zr/Ce precursor salts and polymer were stirred for 24 h. The solution was placed in an open Petri dish for thermal treatment (with water vapor) in the oven at 60 °C, until dried. The samples were identified as Z50AC and Z90AC (50 and 90 mol% CeO$_2$).

Hybrid method (10 mol% Si): 2 g of Pluronic P-123 was previously

* Corresponding author.
E-mail address: rbacani@if.usp.br (R. Bacani).

stirred in 10 mL of ethanol and 1 mL of HCl (2 mol/L). Then 0.15 mL (total 10 mol%) of TEOS (Tetraethyl orthosilicate, Aldrich), the Si precursor, was added dropwise in the solution and stirred together for 30 min. After that 6 mmol of $ZrCl_4$ and $CeCl_3 \cdot 7H_2O$ (Aldrich) were solubilized in another 10 mL of ethanol and added to the polymer mixture (Ce/Zr molar ratio of 0.9). NH_4OH was added to achieve a pH of 3 and the remaining solution was stirred for 24 h. The solution was placed in a Teflon autoclave for hydrothermal treatment in the oven at 60 $^\circ$C for 1 day, and dried in a water bath for 5 h. The sample was identified as Z90H10.

Palisade method (10 and 30 mol% Si): based on the last synthesis, the P-123 polymer and TEOS (total 10 and 30 mol%) were stirred previously for 6 h before adding the same Zr/Ce salt precursors with Ce/Zr molar ratio of 0.9. Then NH_4OH was added to achieve a pH of 3 and the remaining solution was stirred for 24 h. The solution was placed in a Teflon autoclave for hydrothermal treatment in the oven at 60 $^\circ$C for 1 day, and dried in a water bath for 5 h. The samples were identified as Z90P10 and Z90P30.

The calcination process to remove all the samples' template was performed in a tubular oven, with a temperature heating rate of 1 $^\circ$C/min, until 540 $^\circ$C in N_2 atmosphere, an isotherm in 540 $^\circ$C with 2 h in N_2 and 2 h in air.

2.2. ZrO₂-CeO₂ characterization

In-situ Small Angle X-Ray Scattering (SAXS) experiments were carried out at the SAXS-1 beamline of the Brazilian Synchrotron light facility, LNLS. The measurements were performed with Si-(111) crystal as a monochromator, choosing $\lambda = 1.608$ Å. The sample to detector distance was 800 mm and the detector was a bi-dimensional CCD. The oven was programmed for a heating rate of 1 $^\circ$C/min, with an isotherm at 550 $^\circ$C. The sample was set under vacuum ($\sim 10^{-3}$ mbar). The data were normalized by the attenuation factor and the total intensity.

The X-ray powder diffraction (XRD) measurements were carried out at the XPD beamline of the LNLS. The wavelength was set at 1.5498 Å. High-intensity (low-resolution) configuration, without crystal analyzer, was chosen with 2θ from 18° to 102°, with a 0.05° step, and counting times between 2.5 and 3.0 s/step.

2.3. ZrO₂-CeO₂/SiO₂ characterization

The SAXS measurements were carried out using a NANOSTAR (Bruker) sealed Cu tube ($\lambda = 1.5418$ Å) operating at 40 kV and 30 mA, with a multi-filament Hi—STAR bidimensional detector. The point focus geometry was used; the system was collimated by 3 pinholes and a cross-coupled Goebel-mirror system. The set up holds a vacuum path between the sample chamber and the detector. The sample to detector distance was 650 mm, therefore with scattering vector **q** values ranging from $0.012 \, Å^{-1}$ to $0.35 \, Å^{-1}$. All the data were normalized by the measuring time and corrected for absorption effects.

The XRD measurements were performed at an Ultima (Rigaku) equipment with conventional copper tube ($\lambda = 1.5418$ Å), operating at 40 kV and 30 mA, with 2θ from 10° to 100° with a 0.05° step, and counting time of 5 s/step. Rietveld's powder structure refinement analysis was performed for the data of samples calcinated until 540 $^\circ$C. The software Fullprof [19] was used to refine the structural parameters through a least-squares method. The peak shape was assumed to be a pseudo-Voigt function with asymmetry parameters. The background of each pattern was fitted by a 5° polynomial function. Isotropic atomic displacement (temperature) factors were assumed. The least-square method was adopted to minimize the difference between the observed and simulated powder diffraction pattern. The R's values indicated the agreement between the observed and calculated quantities. The refinement was done, reducing R's values and the quality factor goodness of fit (S_{GoF}), until they reach the convergence [20—24].

Nitrogen adsorption isotherms were obtained for all samples (with and without Si) with a NOVA (Quantachrome) porosimeter. Thermal treatment to dry the samples was performed for 2 h at 200 $^\circ$C and measurements were taken in 77 K (N_2). The pore size distribution, pore volume and pore radius were calculated using the BJH method [25]. The specific surface area was calculated using the BET method [26,27].

The cerium oxidation state was evaluated by in situ XANES experiments at the Ce L_{III}-edge. The spectra were collected at the D04B- XAFS1 beamline at the LNLS in transmission mode using a Si(111) monochromator. The samples with SiO_2 were diluted with boron nitride (BN), and pressed into 15 mm diameter pellets (around 4—5 mg of sample and 70 mg of BN). The pellets were placed in a quartz tubular furnace sealed with Kapton windows. These measurements were acquired during temperature-programmed reduction (TPR) process under a 5% H_2/He gas mixture (total flow of 50 mL/min) at temperatures in the range of 25—500 $^\circ$C at a heating rate of 10 $^\circ$C/min. The data were analyzed with the WinXAS software [28].

3. Results and discussion

3.1. ZrO₂-CeO₂

In-situ SAXS experiments were carried out in order to analyze the process of template removal from the samples. Both as-synthesized samples present one diffraction peak, revealing partial spatial correlation between its pores before the calcination process.

For the 50% CeO_2 content (sample Z50AC) this peak decrease as the temperature increases, as shown in Fig. 1. The partially ordered mesopores structure was maintained up to 300 $^\circ$C.

For the 90% CeO_2 content (sample Z90AC), depicted in Fig. 2, the intensity of the peak increased as the temperature increased, reached a maximum around 170 $^\circ$C and then, decreased showing the loss of the ordered mesoporous structure. Fig. 3 shows the radius of gyration (R_G) from Guinier plot [30] (log[I(q)] versus q^2)
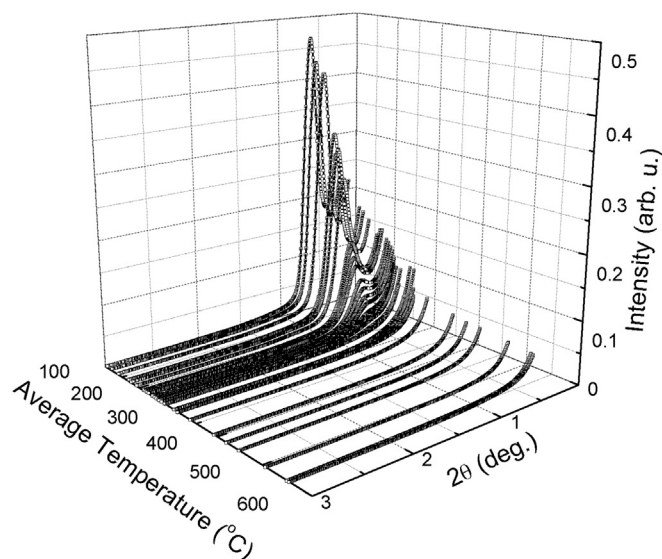

Fig. 1. SAXS curves during the calcination process for the Z50AC sample, with 50% CeO_2.

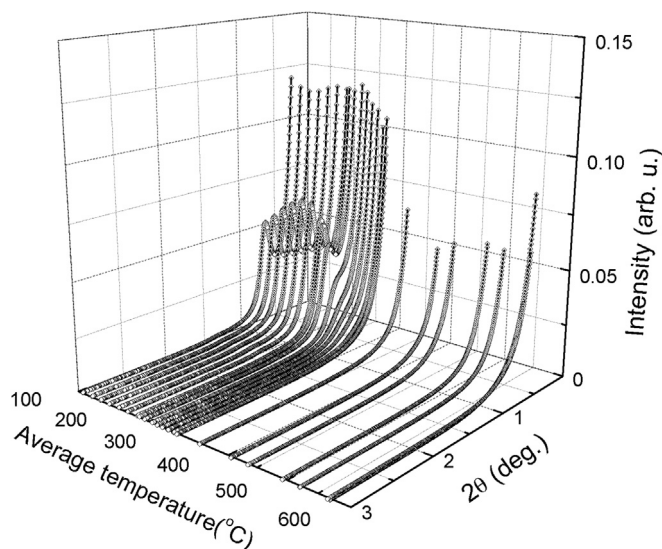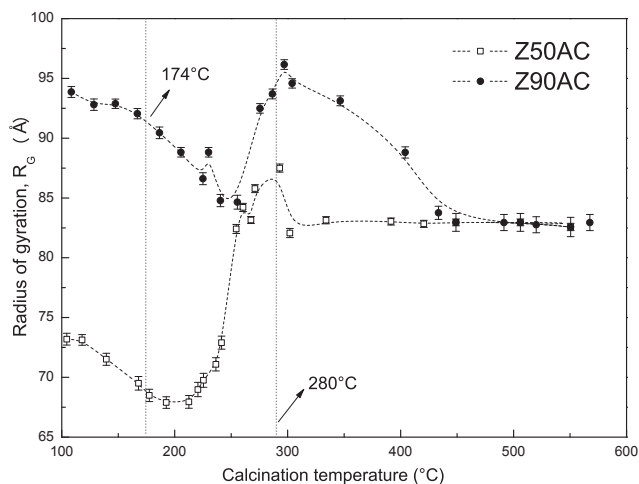**Fig. 2.** SAXS curves during the calcination process for the Z90AC sample, with 90% CeO_2.

Fig. 3. Radius of gyration versus calcination temperature for both samples with different CeO_2 contents.
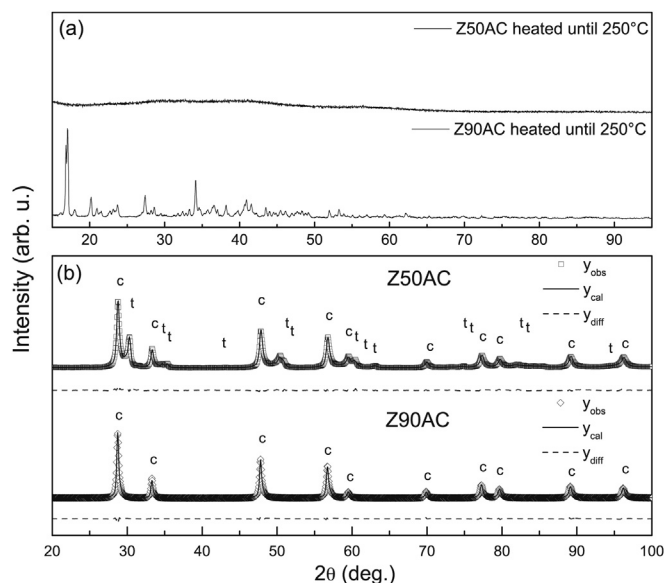

Fig. 4. (a) Conventional XRD patterns for Z50AC and Z90AC heated until 250 °C. (b) Synchrotron XRD pattern of calcined samples at 540 °C (empty symbols) with the Rietveld fitted pattern (line) and the difference plot (dashed line), for Z50AC and Z90AC samples. The "t" denotes the tetragonal structure peaks and "c", the peaks for the cubic structure.

for both CeO_2 contents.

The radius of gyration is related to the mean size of the scattering particles or pores in the sample [29,30]. For mesoporous materials, this parameter can be related to the pore size. Before 174 °C, for both CeO_2 contents, there was a shrinking of the pore size, due to the decomposition of the polymer template, which is expected for SiO_2 systems [31]. Between 200 and 300 °C the radius of gyration increased, suggesting the pores walls were broken. After 300 °C, both samples lost the ordered mesoporous network after the total removal of the polymer (540 °C). At the end of the calcination process there was a final radius of gyration around 80 Å for both ceria contents, showing a shrinkage of the porous structures.

Fig. 4 shows the X-ray powder diffraction results for the Z50AC and Z90AC samples, calcinated until 250 °C and 540 °C.

For Z50AC sample there were no crystalline phases when it was heated until 250 °C. After 540 °C treatment, the crystalline structure was composed of tetragonal ($P4_2/nmc$) and cubic fluorite ($Fm\overline{3}m$) ZrO_2-CeO_2 crystallographic phases [32,33]. For the Z90AC

sample several peaks were observed after it was heated until 250 °C, from chloride and oxychloride phases ($Zr(ClO_4)_4$ and $Ce(ClO_4)_3$[1]). There was a single cubic fluorite type phase ($Fm\overline{3}m$) after calcination until 540 °C.

Rietveld results are presented on Table 1, showing the difference between the two ceria contents. For Z90AC there were larger lattice parameters, leading to a higher cell volume and a larger cubic phase crystallite size. From the lattice parameters it was possible to evaluate the amount of zirconia that was incorporated in to the ZDC lattice [33]. For Z50AC, it was estimated that the compositions of the tetragonal and cubic phases were ZrO_2-15 mol% CeO_2 and CeO_2-5 mol% ZrO_2, respectively. Besides, the fitting results suggested that a small part of amorphous ZrO_2 was still present in this sample.

Nitrogen physisorption results are presented on Fig. 5 and Table 2.

The Z50AC sample presented a type IV isotherm and hysteresis with shape between H_2 and H_3. The BJH pore size distribution (PSD) showed one peak at a mean pore diameter of 28 Å. For higher ceria content, the Z90AC sample, presented hysteresis more characteristic of H_1 type, with capillary condensation happening only at P/P_0 higher values, indicating lower pore sizes and inter-particle porosity contribution. The PSD showed a higher dispersion of pores size for higher ceria content, with medium pore diameter around 21 Å. The BET specific surface area and pore volume were independent of the ceria content. The t-plot analysis showed absence of micropores for both ceria contents. The radius of gyration calculated by SAXS (Fig. 3) was higher than the average pore diameter measured from adsorption, mostly because of inter-particle porosity contribution on the surface adsorption.
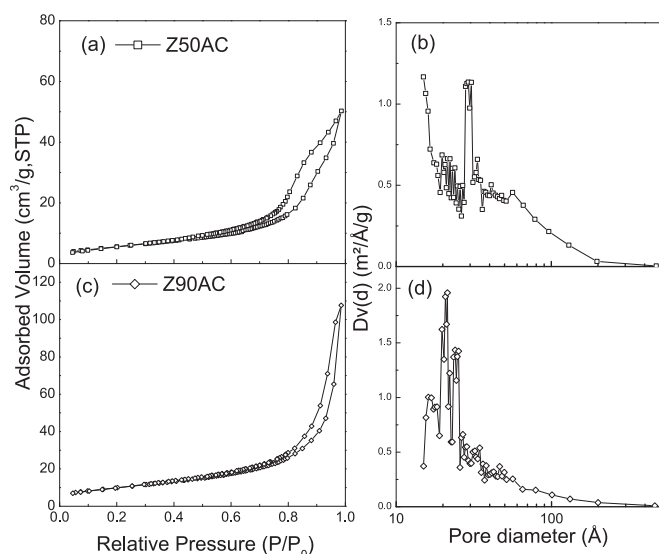
These results indicate that the crystallization process is an important step, which guides the mesoporous structure of these oxides. And, even loosing the ordered porous structure, the ZDC samples present good textural properties for catalysis and SOFC applications.

---

[1] Phases indexed with MDI Jade 6.5 software.

Table 1
Structural parameters of Rietveld analysis for 50 and 90% CeO_2 calcinated samples (until 540 °C). Where a and c are lattice parameters, weight percentage of crystalline phases, V is the lattice volume, D is the average crystallite size. R_p, R_{wp}, R_{exp}, χ^2 and S_{GoF} are the Rietveld standard agreement factors.

	Z50AC		Z90AC
	Cubic	Tetragonal	Cubic
Phase	Fm$\overline{3}$m	P4$_2$/nmc	Fm$\overline{3}$m
	73.2 (4)%	26.84 (9)%	100.0 (6)%
a/Å	5.4089 (15)	3.6215 (5)	5.4090 (6)
c/Å	−	5.2160 (5)	−
V/Å^3	158.236 (8)	68.41 (7)	158.364 (3)
D/nm	16.3 (3)	6.63 (9)	29.8 (9)
R_p	7.31		6.82
R_{wp}	7.57		6.05
R_{exp}	2.45		2.90
χ^2	9.56		5.3
S_{GoF}	3.1		2.1

Fig. 5. Nitrogen physisorption isotherm and the pore size distribution (PSD, right) calculated from the adsorption branch using the BJH method for: (a) isotherm and (b) PSD, for Z50AC sample. (c) isotherm and (d) PSD, for Z90AC sample.
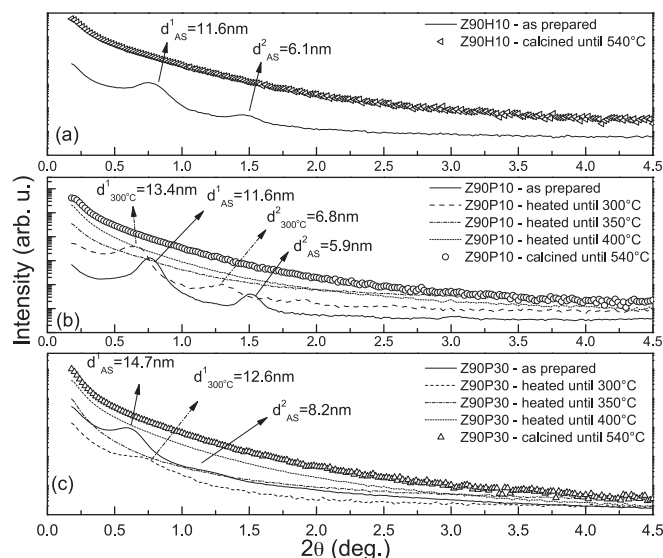
Table 2
Nitrogen physisorption results: Specific surface area S_{BET}, pore volume V_P, mean pore diameter D_P.

Samples	S_{BET} (m^2/g)	V_P (cm^3/g)	D_P (Å)
Z50AC	47.3	0.18	28
Z90AC	46.1	0.21	21

3.2. ZrO_2-CeO_2/SiO_2

In order to increase the mechanical stability of these ZDC systems, two different one-pot synthesis with low SiO_2 content and 90% CeO_2 (single phase cubic structure), were tested (sec. 2). The SAXS results are shown on Fig. 6 and Table 3, with results before and after calcination for all samples.

Since the first sample from hybrid method (Z90H10) showed a disordered porous structure after calcination until 540 °C, the samples from palisade method (Z90P10 and Z90P30) were heated until intermediate temperatures (300, 350 and 400 °C) in order to evaluate the ordered porous structure evolution. The presence of several peaks at the low angle/scattering vector region of SAXS measurements indicates that the material has an ordered porous structure and, more than one peak indicates which structure was

Fig. 6. SAXS curves for (a) Z90H10 as prepared and calcined. Ex-situ SAXS experiment for: (a) Z90P10 and, (b) Z90P30.

Table 3
SAXS parameters: Area under the peaks A_P, total area under the SAXS curve A_T, ordering factor f, where $f = A_P/A_T$, and radius of gyration, R_G.

Samples	A_P (arb. u.)	A_T (arb. u.)	f	R_G (Å)
Z90H10				
as prepared	14	39	0.36	124.2
calcined	−	7184	0	114.3
Z90P10				
as prepared	19	26	0.71	112.7
300 °C	63	107	0.51	90.9
350 °C	−	442	0	117.5
400 °C	−	1954	0	128.7
calcined	−	5126	0	114.6
Z90P30				
as prepared	73	298	0.24	112.6
300 °C	2	30	0.07	118.6
350 °C	−	807	0	136.7
400 °C	−	4187	0	125.5
calcined	−	9476	0	132.6

formed after the synthesis.

The ordering factor f was defined as the area of the peaks after subtracting the scattering baseline (A_P) divided by the total area under the peaks without the baseline removal (A_T), so $f = A_P/A_T$. Since the area under the SAXS curve is proportional to the scattering pores/particles, it was possible to compare samples having

higher ordering, relying on the pore structure.

Studying the interplanar distances from uncalcined samples in Fig. 6, the results obtained for samples prepared by the hybrid and palisade methods were similar. Comparing interplanar distances d^1 from the first peak and d^2 for the second peak, it was possible to index a lamellar structure where the lattice parameter for the pores, a_p, is $1/d_{h0} = h/a_p$. Therefore $a \sim d^1_{10} = 116\,\text{Å}$ for Z90H10 and Z90P10. The sample Z90P30 presents two peaks, closer to a 2D hexagonal structure with average lattice parameter $a_p = 180\,\text{Å}$, calculated using $\frac{1}{d^2_{hk0}} = \frac{4}{3}\frac{h^2+hk+k^2}{a^2_p}$ (for this case, hkl is equal to 100 and 200).

From hybrid and palisade method with 10 mol% Si it was possible to infer that stirring the polymer and TEOS prior to Zr/Ce addition during preparation resulted in higher ordering factor. As the temperature increased, the total area increased, since the intensity of SAXS depends mostly on the structure density contrasts. Both samples of the palisade method maintained their ordered porous network until 350 °C, where there were no more peaks on the SAXS curves. The ordering factor decreased as the temperature increased. The radius of gyration for Z90P10 decreased at 300 °C, indicating a abrupt shrinkage of the structure, while for Z90P30 the radius increased at 350 °C which could suggest the rupture of the walls of the 2D hexagonal structure.

Fig. 7 shows the diffraction patterns for calcined Z90H10. The Z90P10 and Z90P30 samples were analyzed after heat treatments up to 300, 350, 400 °C and calcined (540 °C). Rietveld results are presented on Table 4.

The XRD measurements were obtained for the same temperatures analyzed by SAXS experiments, in order to study what undergoes with the increase of the temperature and the crystalline structure.

For Z90P10 the crystallization started only at 350 °C, later than previous sample with the same ceria content. Z90P30 at 350 °C presented an amorphous pattern, showing a even later crystallization, at 400 °C. Sample Z90H10 showed a smaller crystallite size. From Rietveld results there were no significant changes on the overall crystallographic structure of the ZDC synthesized with Si, the lattice parameters are similar from cubic single-phase solid solutions synthesized by gel-combustion routes [33].

N_2 physisorption results are presented on Fig. 8 and Table 5.

Hybrid method sample resulted in a type H_4 hysteresis, while both palisade samples presented hysteresis loops that could be identified between the H_2 and H_3 types. From PSD curves a higher silica content resulted in a narrower pore size distribution.

From the t-plot analysis [34], micropores were detected in the Z90H10 sample ($V_p t-plot = 0.012\,\text{cm}^3/\text{g}$ and $S^{t-plot} = 8.1\,\text{m}^2/\text{g}$), while Z90P10 and Z90P30 only presented mesopores. The addition of the Zr/Ce precursors after the previous P-123 and TEOS solution resulted in a higher surface area, but slightly lower pore volume. Higher silica content resulted in higher surface area and pore volume, showing the advantage of a silica palisade to improve the material texture.

In situ XANES results are presented on Fig. 9. The analysis method described by Zhang et al. [35] was used to quantify the fraction of Ce^{3+} in the samples. It consists of a least-squares fit of the experimental data with the WinXAS software, using four Gaussian profiles and one arctangent function (Fig. 9, inset) [28].

Pure CeO_2 spectrum at L_{III}-edge has two main peaks, A and B, which are related with Ce^{4+} final states from 2p to 5d transitions. The peak C occurs due to dipole transitions and it is characteristic of the Ce trivalent state. The pre-edge peak D corresponds to multiple scattering processes [35–38]. Therefore the Ce^{3+} fraction is equal to the relation of the peak areas, such that C/(A + B + C), where A, B and C represent the area of the fitted peaks. Fig. 9 shows that with the increase of temperature under reduction conditions promoted a shift from Ce^{4+} to Ce^{3+}. At 500 °C the Z90P10 sample reached a percentage reduction of 28%, and the Z90P30, 54%.
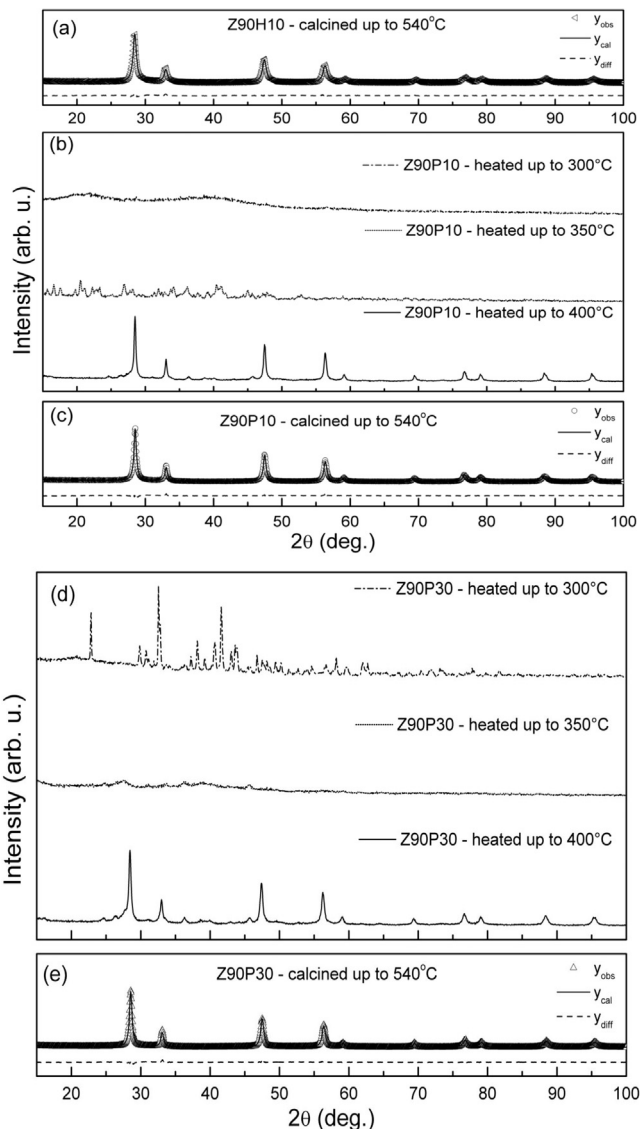

Fig. 7. XRD for (a) Z90H10, calcined. Ex-situ XRD experiment for: (b) Z90P10, (c) Z90P10, calcined. Ex-situ XRD experiment for: (d) Z90P30, (e) Z90P30, calcined. Symbols represents experimental data, with the Rietveld fitted pattern (line) and the difference plot (dashed line) for calcined samples.

Table 4
Structural parameters of Rietveld analysis for 90% CeO_2 (Z90H10, Z90P10 and Z90P30) calcinated samples (until 540 °C). Where a and c are lattice parameters, weight percentage of crystalline phases, V is the lattice volume, D is the average crystallite size. R_p, R_{wp}, R_{exp}, χ^2 and S_{GoF} are the Rietveld standard agreement factors.

|	Z90H10	Z90P10	Z90P30
	Cubic	Cubic	Cubic
Phase	$Fm\bar{3}m$	$Fm\bar{3}m$	$Fm\bar{3}m$
	100.0 (7)%	100.0 (5)%	100.0 (8)%
a/Å	5.4150 (14)	5.4089 (11)	5.4094 (11)
V/Å³	158.38 (7)	158.24 (6)	158.29 (6)
D/nm	18.59 (9)	29.5 (4)	27.7 (3)
R_p	8.24	9.71	9.19
R_{wp}	10.5	12.0	11.9
R_{exp}	5.15	5.74	5.85
χ^2	4.2	4.4	4.1
S_{GoF}	1.9	2.1	2.0
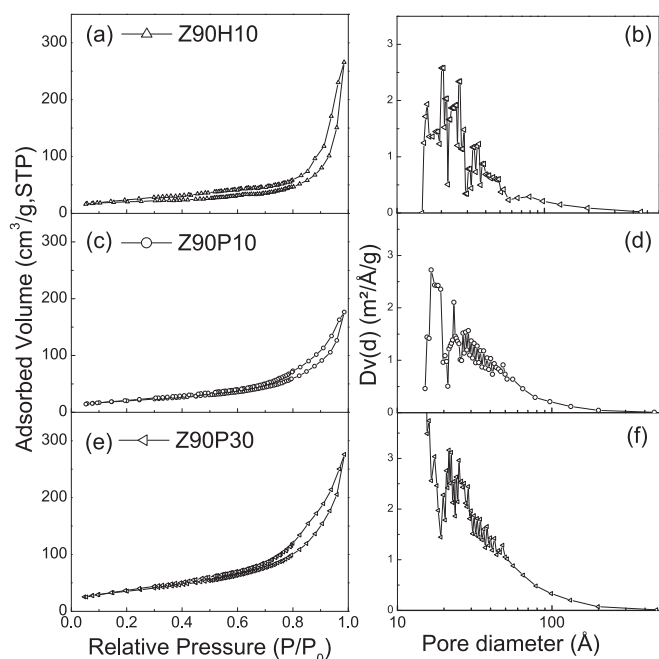
Fig. 8. Nitrogen physisorption isotherms and the PSD for: Z90H10 (a) isotherm, and (b) PSD. Z90P10 (c) isotherm, and (d) PSD. Z90P30 (e) isotherm, and (f) PSD.

Table 5
Nitrogen adsorption results: Specific surface area S_{BET}, pore volume V_P, mean pore diameter D_P.

Samples	S_{BET} (m²/g)	V_P (cm³/g)	D_P (Å)
Z90H10	67.5	0.43	23
Z90P10	72.7	0.27	26
Z90P30	128.2	0.41	24
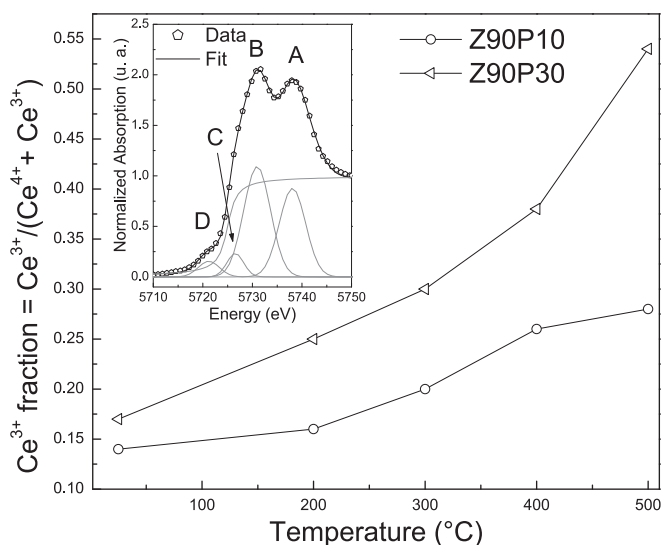
Fig. 9. Ce^{3+} fraction for Z90P10 and Z90P30 samples as a function of the temperature, under temperature programmed reduction process (TPR) with 5% H$_2$/He. Inset shows the CeO$_2$ XANES spectrum at Ce L$_{III}$-edge.

Although the total reduction of Ce^{3+} to Ce^{4+} was not achieved in the studied temperature range, the increase of the silica content from 10 to 30 mol% and the improvement on the superficial area

(from 73 to 120 m²/g, respectively) promoted a higher reduction of Ce^{4+} under lower temperatures compared to materials synthesized via gel-combustion routes [38,39].

4. Conclusions

In this work new synthetic routes of ZDC were reported, using soft template methods. Three new synthesis methods with low SiO$_2$ content were developed to increase mechanical stability of the pores. The lack of an ordered structure of the pores was correlated to the amorphous-crystalline transition of ZrO$_2$-CeO$_2$ at 300 °C. Although there were no ordered pores, the samples showed proper textural properties for applications in catalysis, as well as SOFC anodes. A higher pore ordering was obtained and kept up to 350 °C, compared to other materials in the literature. Appropriate textural properties were obtained, specially higher specific surface area. And finally, in situ XANES results revealed a high reduction rate of Ce^{3+} to Ce^{4+} at 500 °C under TPR, which is directly correlated to higher catalytical activity.

References

[1] D. Gu, F. Schüth, Synthesis of non-siliceous mesoporous oxides, Chem. Soc. Rev. 43 (2014) 313—344, http://dx.doi.org/10.1039/c3cs60155b.
[2] C.T. Kresge, M.E. Leonowicz, W.J. Roth, J.C. Vartuli, J.S. Beck, Ordered mesoporous molecular sieves synthesized by a liquid-crystal template mechanism, Nature 359 (6397) (1992) 710—712, http://dx.doi.org/10.1038/359710a0.
[3] J.S. Beck, J.C. Vartuli, W.J. Roth, M.E. Leonowicz, C.T. Kresge, K.D. Schmitt, C.T.W. Chu, D.H. Olson, E.W. Sheppard, A new family of mesoporous molecular sieves prepared with liquid crystal templates, J. Am. Chem. Soc. 114 (27) (1992) 10834—10843, http://dx.doi.org/10.1021/ja00053a020.
[4] A. Sayari, P. Liu, Non-silica periodic mesostructured materials: recent progress, Microporous Mesoporous Mater. 12 (4) (1997) 149—177, http://dx.doi.org/10.1016/S0927-6513(97)00059-X.
[5] U. Ciesla, F. Schüth, Ordered mesoporous materials, Microporous Mesoporous Mater. 27 (1999) 131—149, http://dx.doi.org/10.1016/S1387-1811(98)00249-2.
[6] A. Taguchi, F. Schüth, Ordered mesoporous materials in catalysis, Microporous Mesoporous Mater. 77 (2005) 1—45, http://dx.doi.org/10.1016/B978-0-12-385516-9.00002-8.
[7] P. Fornasiero, G. Balducci, R.D. Monte, J. Kaspar, V. Sergo, G. Gubitosa, A. Ferrero, M. Graziani, Modification of the redox behaviour of CeO$_2$ induced by structural doping with ZrO$_2$, J. Catal. 164 (1996) 173—183, http://dx.doi.org/10.1006/jcat.1996.0373.
[8] G. Vlaic, R.D. Monte, P. Fornasiero, E. Fonda, J. Kaspar, M. Graziani, The CeO$_2$—ZrO$_2$ system: Redox properties and structural relationships., Stud. Surf. Sci. Catal. 116 (1998) 185—195, http://dx.doi.org/10.1016/S0167-2991(98)80876-8.
[9] H. Vidal, J. Kaspar, M. Pijolat, G. Colon, S. Bernal, A. Cordón, V. Perrichon, F. Fally, Redox behavior of CeO$_2$—ZrO$_2$ mixed oxides I. influence of redox treatments on high surface area catalysts, Appl. Catal. B Environ. 27 (2000) 49—63, http://dx.doi.org/10.1016/S0926-3373(00)00138-7.
[10] R.D. Monte, J. Kaspar, Nanostructured CeO$_2$—ZrO$_2$ mixed oxides, J. Mater. Chem. 15 (2005) 633—648, http://dx.doi.org/10.1039/B414244F.
[11] D. Lamas, S. Bianchetti, M. Cabezas, N.E.W. de Reca, Nanostructured ceramic materials: Applications in gas sensors and solid-oxide fuel cells, J. Alloy. Compd. 495 (2010) 548—551, http://dx.doi.org/10.1016/j.jallcom.2009.10.014.
[12] M. Melchionna, P. Fornasiero, The role of ceria-based nanostructured materials in energy applications, Mater. Today 17 (7) (2014) 349—357, http://dx.doi.org/10.1016/j.mattod.2014.05.005.
[13] P.D. Yang, D.Y. Zhao, D.I. Margolese, B.F. Chmelka, G.D. Stucky, Block copolymer templating syntheses of mesoporous metal oxides with large ordering lengths and semicrystalline framework, Chem. Mater. 11 (1999) 2813—2826, http://dx.doi.org/10.1021/cm990185c.
[14] F. Zhang, C.-H. Chen, J.C. Hanson, R.D. Robinson, I.P. Herman, S.-W. Chan, Phases in ceria—zirconia binary oxide $_{(1-x)}$ CeO$_2$—xZrO$_2$ nanoparticles: The effect of particle size, J. Am. Ceram. Soc. 89 (3) (2006) 1028—1036, http://

dx.doi.org/10.1111/j.1551-2916.2005.00788.x.

[15] Q. Yuan, Q. Liu, W.-G. Song, W. Feng, W.-L. Pu, L.-D. Sun, Y.-W. Zhang, C.-H. Yan, Ordered mesoporous $Ce_{1-x}Zr_xO_2$ solid solutions with crystalline walls, J. Am. Chem. Soc. 129 (2007) 6698—6699, http://dx.doi.org/10.1021/ja070908q.

[16] B.M. Reddy, P. Bharali, Y.-H. Seo, E.A. Prasetyanto, S.-E. Park, Surfactant-controlled and microwave-assisted synthesis of highly active $CexZr_{1-x}O_2$ nano-oxides for co oxidation, Catal. Lett. 126 (2008) 125, http://dx.doi.org/10.1007/s10562-008-9591-5.

[17] Y. Quan, L.-L. Li, S.-L. Lu, H.-H.L. Duan, Zhen-Xing, Y.-X. Zhu, C.-H. Yan, Facile synthesis of Zr-based functional materials with highly ordered mesoporous structures, J. Phys. Chem. C 113 (2009) 4117—4124, http://dx.doi.org/10.1021/jp806467c.

[18] H. Li, L. Zhang, H. Dai, H. He, Facile synthesis and unique physicochemical properties of three-dimensional ordered macroporous magnesium oxide, gamma-alumina, and ceria-zirconia solid solutions with crystalline meso-porous walls, Inorg. Chem. 48 (2009) 4421—4433, http://dx.doi.org/10.1021/ic900132k.

[19] J. Rodriguez-Carbajal, Fullprof Suite; Version 3.5d, Institute Laue-Langevin, Grenoble, France, 2009-2012.

[20] R.A. Young, The Rietveld Method (International Union of CrystalLography Monographs on Crystal), Oxford University Press, USA, 1995.

[21] L.B. McCusker, R.B.V. Dreele, D.E. Cox, D. Loueor, P. Scardi, Rietveld refinement guidelines, J. Appl. Crystallogr. 32 (1999) 36—50, http://dx.doi.org/10.1107/S0021889898009856.

[22] E. Jansen, W. Schafer, G. Will, R values in analysis of powder diffraction data using Rietveld refinement, J. Appl. Crystallogr. 27 (1993) 492—496, http://dx.doi.org/10.1107/S0021889893003267.

[23] R.J. Hill, R.X. Fischer, Profile agreement indices in Rietveld and pattern-fitting analysis, J. Appl. Crystallogr. 23 (1990) 462—468, http://dx.doi.org/10.1107/S0021889890006094.

[24] J.-F. Bérar, P. Lelann, E.S.D.'s and estimated probable error obtained in Rietveld refinements with local correlations, J. Appl. Crystallogr. 24 (1991) 1—5, http://dx.doi.org/10.1107/S0021889890008391.

[25] E.P. Barrett, L.G. Joyner, P.P. Halenda, The determination of pore volume and area distributions in porous substances. I. computations from nitrogen iso-therms, J. Am. Chem. Soc. 73 (1) (1951) 373—380, http://dx.doi.org/10.1021/ja01145a126.

[26] S. Brunauer, P.H. Emmet, E. Teller, Adsorption of gases in multimolecular layers, J. Am. Chem. Soc. 60 (1938) 309—319, http://dx.doi.org/10.1021/ja01269a023.

[27] K.S.W. Sing, D.H. Everett, R.A.W. Haul, L. Moscou, R.A. Pierotti, J. Rouquérol, T. Siemieniewska, Reporting physisorpion data for gas/solid systems with special reference to the determination of surface area and porosity, Pure Appl.

Chem. 57 (1985) 603—619.

[28] T. Ressler, WinXAS: a program for X-ray absorption spectroscopy data anal-ysis under MS-Windows, J. Synchrotron Radiat. 5 (1998) 118—122, http://dx.doi.org/10.1107/S0909049597019298.

[29] A.F. Craievich, Small-angle X-ray Scattering by Nanostructured Materials - Handbook of Sol-gel Science and Technology - Volume II: Materials Charac-terization. Chapter 8, Kluwer Academic Publishers, 2005.

[30] A. Guinier, G. Fournet, Small-angle Scattering of X-rays, John Wiley and Sons, New York, 1955.

[31] F. Kleitz, W. Schmidt, F. Schüth, Evolution of mesoporous materials during the calcination process: Structural and chemical behavior, Microporous Meso-porous Mater. 44—45 (2001) 95—109, http://dx.doi.org/10.1016/S1387-1811(01)00173-1.

[32] S. Rossignol, F. Gerard, D. Duprez, Effect of the preparation on the properties of zirconia-ceria materials, J. Mater. Chem. 9 (1999) 1615—1620, http://dx.doi.org/10.1039/A900536F.

[33] D.G. Lamas, R.O. Fuentes, I.O. Fábregas, M.E.F. de Rapp, G.E. Lascalea, J.R. Casanova, N.E.W. de Reca, A.F. Craievich, Synchrotron X-ray diffraction study of the tetragonal-cubic phase boundary of nanocrystalline ZrO_2-CeO_2 synthesized by a gel-combustion process, J. Appl. Crystallogr. 38 (2005) 867—873, http://dx.doi.org/10.1107/S0021889805025343.

[34] B.C. Lippens, J.H. de Boer, Studies on pore systems via the t method, J. Catal. 4 (1965) 319—323, http://dx.doi.org/10.1016/0021-9517(65)90263-0.

[35] F. Zhang, P. Wang, J. Koberstein, S. Khalid, S.-W. Chan, Cerium oxidation state in ceria nanoparticles studied with x-ray photoelectron spectroscopy and absorption near edge spectroscopy, Surf. Sci. 563 (2004) 74—82, http://dx.doi.org/10.1016/j.susc.2004.05.138.

[36] H. Yoshida, L. Yuliati, T. Hamajima, T. Hattori, Valence of highly dispersed cerium oxide species on silica quantitatively estimated by Ce L_{III}-edge XANES, Mater. Trans. 45 (2004) 2062—2067, http://dx.doi.org/10.2320/matertrans.45.2062.

[37] A.M. Shahin, F. Grandjean, G.J. Long, T.P. Schuman, Cerium L_{III}-Edge XAS investigation of the structure of crystalline and amorphous cerium oxides, Chem. Mater. 17 (2005) 315—321, http://dx.doi.org/10.1021/cm0492437.

[38] L.M. Acuna, F.F. Munoz, M.D. Cabezas, D.G. Lamas, A.G. Leyva, M.C.A. Fantini, R.T. Baker, R.O. Fuentes, Improvement in the reduction behavior of novel ZrO_2—CeO_2 solid solutions with a tubular nanostructure by incorporation of Pd, J. Phys. Chem. C 114 (2010) 19687—19696, http://dx.doi.org/10.1021/jp108429t.

[39] M. Zimicz, S.A. Larrondo, R.J. Prado, D.G. Lamas, Time-resolved in situ XANES study of the redox properties of $Ce_{0.9}Zr_{0.1}O_2$ mixed oxides, Int. J. Hydrogen Energy 37 (19) (2012) 14881—14886, http://dx.doi.org/10.1016/j.ijhydene.2012.01.162.